

## Mueller matrix polarimetry for the characterization of complex random medium like biological tissues

NIRMALYA GHOSH<sup>1,\*</sup>, JALPA SONI<sup>1</sup>, M F G WOOD<sup>2</sup>, M A WALLENBERG<sup>2</sup>  
and I A VITKIN<sup>2</sup>

<sup>1</sup>Department of Physical Sciences, Indian Institute of Science Education and Research,  
Kolkata 741 252, India

<sup>2</sup>Department of Medical Biophysics, University of Toronto, Toronto, Ontario, Canada

\*Corresponding author. E-mail: nghosh@iiserkol.ac.in

**Abstract.** The polarization parameters of light scattered from biological tissues contain wealth of morphological and functional information of potential biomedical importance. But, in optically thick turbid media such as tissues, numerous complexities due to multiple scattering and simultaneous occurrences of many polarization events present formidable challenges, in terms of both accurate measurement and unique interpretation of the individual polarimetry characteristics. We have developed and validated an expanded Mueller matrix decomposition approach to overcome this problem. The approach was validated theoretically with a polarization-sensitive Monte Carlo light propagation model and experimentally by recording Mueller matrices from tissue-like complex random medium. In this paper, we discuss our comprehensive turbid polarimetry platform consisting of the experimental polarimetry system, forward Monte Carlo modelling and inverse polar decomposition analysis. Initial biomedical applications of this novel general method for polarimetry analysis in random media are also presented.

**Keywords.** Scattering; polarization; Mueller matrix; wave propagation in random media; biomedical applications.

**PACS Nos** 42.68.Mj; 42.25.Ja; 42.25.Dd; 42.62.Be

### 1. Introduction

Development of optical techniques for biomedical diagnosis is an area of considerable current research interest as optical methods can facilitate non-invasive and quantitative diagnosis [1]. For optical diagnosis, one generally exploits the scattered (both elastically and inelastically) light from biological tissues. The inelastically scattered light (via processes like fluorescence and Raman) contains useful biochemical information on the sample that can be exploited for probing subtle biochemical changes as a signature of disease progression. Elastically scattered light from the tissue also contains rich morphological and functional information of potential biomedical importance. Motivated by this fact, various optical techniques based on scattered light (elastically or inelastically) from tissues are being actively pursued for their diagnostic potential [1,2]. Recently, the polarimetric approaches have also

received considerable attention in biomedical diagnosis [3] because polarization parameters of light scattered from tissues contain additional diagnostic information which cannot be obtained from polarization blind measurements. For example, the anisotropic organized nature of many tissues stemming from their fibrous structure leads to linear birefringence (or linear retardance). Muscle fibres and extra-cellular matrix proteins (such as collagen and elastin) possess fibrous structure and accordingly exhibit linear birefringence. Changes in the fibrous structure from disease progression or treatment response alter the optical birefringence properties, making this a potentially sensitive probe of tissue status [4,5]. Similarly, glucose, present in tissues, exhibits circular birefringence because of its chiral structure. This leads to rotation of the plane of linearly polarized light about the axis of propagation (known as optical rotation or optical activity). Measurements of optical rotation may also offer an attractive approach for non-invasive monitoring of tissue glucose levels [6,7]. Despite the wealth of interesting properties that can be probed with polarized light, in optically thick turbid media such as tissues, numerous complexities due to multiple scattering hinder measurement and data interpretation. Multiple scattering causes extensive depolarization that confounds the traditional polarimetric techniques. Further, even if some residual polarization signal can be measured, multiple scattering alters the polarization state in a complex fashion, for example by scattering-induced diattenuation (dichroism) and by scattering-induced changes in orientation of the polarization vector [7,8]. A further complexity in quantitative polarimetry in tissues arises due to simultaneous occurrences of many polarization events (most common tissue polarimetry events are depolarization, linear birefringence and optical activity). Methods to account (or compensate) for the effects of multiple scattering, and to decouple the individual contributions of several effects occurring simultaneously, are thus needed.

The Mueller matrix represents the transfer function of an optical system in its interactions with polarized light and it contains complete information about all the medium polarization properties [9,10]. But, when many optical polarization effects occur simultaneously (as is the case for tissues), the resulting Mueller matrix elements are contributed by complex and interrelated combinations of these polarization events. These therefore represent several ‘lumped’ effects, masking potentially interesting ones and hindering their interpretation. Each of the individual polarimetry characteristics, if separately extracted/quantified, can potentially serve as useful biological metric. We have thus recently explored the use of an expanded Mueller matrix decomposition approach to delineate individual intrinsic tissue polarimetry characteristics. The approach was validated theoretically with a polarization-sensitive Monte Carlo (MC) simulation model (capable of simulating all the simultaneous optical scattering and polarization effects) and experimentally by recording Mueller matrices from complex tissue-like turbid medium. In this paper, we shall briefly review our comprehensive turbid polarimetry platform consisting of the experimental polarimetry system, forward Monte Carlo modelling and inverse polar decomposition analysis [11–14]. Selected results of the validation studies, initial biomedical applications for monitoring regenerative treatments of the heart as well as initial *in vivo* demonstration, will be discussed.

## 2. Comprehensive turbid medium polarimetry platform

### 2.1 Experimental polarimetry system

Our turbid polarimetry platform consists of three components: (i) high sensitivity experimental polarimetry system, (ii) polarization-sensitive forward Monte Carlo model and (iii) the inverse polar decomposition analysis. Here, we briefly describe our experimental polarimetry system. The polarization-sensitive Monte Carlo model and the inverse polar decomposition analysis are discussed subsequently in §§2.2 and 2.3 respectively.

The experimental polarimetry system consists of both point measurement and large area imaging systems. The point polarimetry system provides a high signal-to-noise ratio (SNR) polarimetric signal, whereas the imaging system, although suffering from a higher SNR, allows for spatial mapping of polarization parameters from a sample. A schematic of the point measurement system is shown in figure 1a. The details of the experimental system have been reported previously [11]. Briefly, the polarization states (of a He-Ne laser at 632.8 nm) are controlled using a polarizer ( $P_1$ ) and quarter-wave plate ( $QWP_1$ ) combination, enabling either linear or circular incidence. After interacting with the sample, light in a user-selected angle is collected with a lens ( $L_1$ ) and passes through a removable quarter-wave plate ( $QWP_2$ ) oriented at  $-45^\circ$  and then through a photoelastic modulator (PEM, Hinds Instruments, IS-90) operating at a frequency  $f_p = 50$  kHz. Finally, the light passes through a linear analyzer ( $P_2$ ) oriented at  $45^\circ$ , converting the polarization-modulated light into intensity-modulated light at 50 kHz (and its harmonic at 100 kHz), and is detected with an avalanche photodiode (APD, Hamamatsu, C5460). The resulting photocurrent is then sent to a lock-in amplifier for synchronous detection. The details of the signal analysis procedure can be found in refs [11,15]. Briefly, the first and second harmonics of the lock-in detected signals can be used to determine the four Stokes parameters ( $[I Q U V]$ ), for any given incident state of polarization. The complete Mueller matrix can be obtained by cycling the input polarization between four states (linear polarization at  $0^\circ$ ,  $45^\circ$ ,  $90^\circ$ , and right circular polarization), measuring the output Stokes vector for each respective input state, and performing simple algebraic manipulations [11].

A schematic of the polarimetry imaging system is shown in figure 1b. Light from a 635-nm diode laser (ThorLabs) is used as the excitation source here. The polarization state of the incident light is controlled using a removable quarter-wave plate and a linear polarizer (polarization state generator, PSG). As the beam exits the sample, a removable quarter-wave plate and linear analyzer (polarization state analyzer, PSA) select a single polarization state of the outgoing light, which is finally detected with a CCD camera (CoolSNAP K4, Photometrics,  $2048 \times 2048$  pixels,  $7.4 \times 7.4 \mu\text{m}^2$  pixel size). Four input states (horizontal, vertical,  $+45^\circ$ , right-circularly polarized) and six output states (horizontal, vertical,  $\pm 45^\circ$ , right- and left-circularly polarized light) were recorded for a total of 24 combinations of measurements. The output Stokes parameters for each input state were measured from the detected intensities as [9]

$$I = I_{180^\circ} + I_{90^\circ},$$

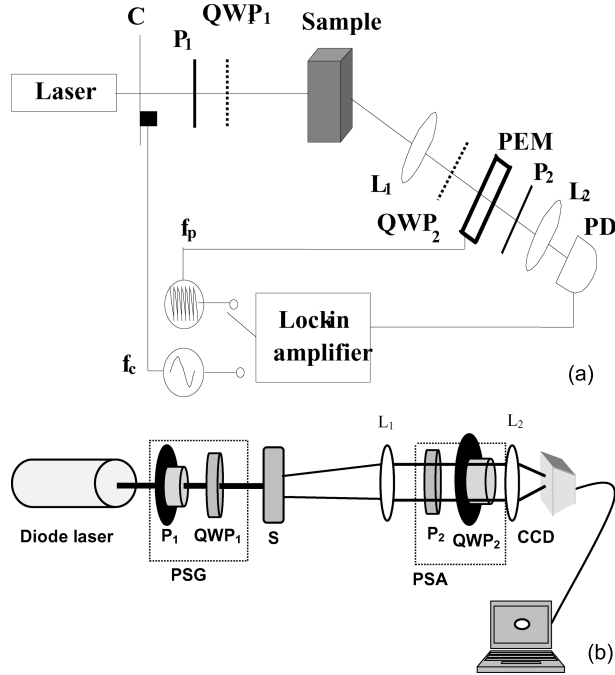


**Figure 1.** (a) Schematic of the point measurement polarimetry system. C: mechanical chopper; P<sub>1</sub>, P<sub>2</sub>: polarizers; QWP<sub>1</sub>, QWP<sub>2</sub>: removable quarter-wave plates; L<sub>1</sub>, L<sub>2</sub>: lenses; PEM: photoelastic modulator; PD: photodetector; f<sub>c</sub>, f<sub>p</sub>: modulation frequencies of mechanical chopper and PEM, respectively. (b) Schematic of the polarimetry imaging system. P<sub>1</sub>, P<sub>2</sub>: polarizers; QWP<sub>1</sub>, QWP<sub>2</sub>: quarter-wave plates and L<sub>1</sub>, L<sub>2</sub>: lenses.

$$\begin{aligned} Q &= I_{180^\circ} - I_{90^\circ}, \\ U &= I_{45^\circ} - I_{135^\circ}, \\ V &= I_R - I_L, \end{aligned} \quad (1)$$

where the subscripts indicate the output state being detected (as determined by the presence or absence of the quarter-wave plate, and the orientation of the analyser). Finally, the 16 elements of the Mueller matrix were determined in a manner similar to that for the point measurement system [11].

## 2.2 Monte Carlo model for polarized light propagation in random medium

Monte Carlo technique is a general and robust approach for modelling light transport in random medium [16]. In this modelling, it is assumed that scattering events occur independently and exhibit no coherence effects. The position, propagation direction and polarization of each photon are initialized and modified as the photon propagates through the scattering medium. The photon propagates in the sample

between scattering events at a distance  $l$  sampled from the probability distribution  $\exp(-\mu_t l)$ . Here, the extinction coefficient  $\mu_t$  is the sum of the absorption  $\mu_a$  and scattering  $\mu_s$  coefficients and  $l$  is the distance travelled by the photon between scattering events [16]. When the photon encounters a scattering event, a scattering plane and angle are statistically sample-based on the polarization state of the photon and the Mueller matrix of the scatterer calculated through Mie scattering theory [17,18]. The photon's reference frame is first expressed in the scattering plane and then transformed to the laboratory (experimentally observable) frame. The polarization information (in the form of Stokes vectors) is tracked for each photon packet. The scattering histories of a large number of such packets are tracked as they propagate through the medium and are summed to yield the macroscopic polarization parameters of interest (Stokes vectors, Mueller matrices, pathlength distributions, polarization statistics from different scattering histories etc.).

Simulations were run for a set of input optical parameters of the scattering medium ( $\mu_s$  and  $\mu_a$ ) exhibiting simultaneous linear and circular birefringence effects. In the simulations, circular and linear birefringence were modelled through the optical activity  $\chi$  in degrees per centimeter, and through the anisotropy in refractive indices ( $\Delta n$ ), respectively. Here,  $\Delta n$  ( $= n_e - n_o$ ) is the difference in refractive index along the extraordinary axis ( $n_e$ ) and the ordinary axis ( $n_o$ ). For simplicity, the direction of the extraordinary axis and the value for  $\Delta n$  were assumed as constants throughout the scattering medium. In each simulation,  $n_e$  and  $n_o$  were given as input parameters and a specific direction of the extraordinary axis was chosen. The Mueller matrices were generated for a slab of scattering medium having varying optical properties ( $\mu_s$ ,  $\Delta n$  and  $\chi$ ), for light exiting the medium through any user-selected direction. The absorption was taken to be small ( $\mu_a = 0.001 \text{ cm}^{-1}$ ) for all simulations. The photon collection geometry was chosen to have a detection area of  $1 \text{ mm}^2$  and an acceptance angle of  $20^\circ$  (parameters mimicking our experimental polarimetry system [11]).

### 2.3 The inverse Mueller matrix decomposition analysis

The key component of our turbid polarimetry platform is the Mueller matrix decomposition approach for solving the complicated inverse problem. This involves extraction of constituent polarization properties from a given 'lumped' system Mueller matrix of any unknown complex system. This method consists of decomposing a given Mueller matrix  $\mathbf{M}$  into the product of three 'basis' matrices [11,19],

$$\mathbf{M} \Leftarrow \mathbf{M}_\Delta \cdot \mathbf{M}_R \cdot \mathbf{M}_D \quad (2)$$

with  $\Leftarrow$  symbol signifying the decomposition process. Here, the matrix  $\mathbf{M}_\Delta$  describes the depolarizing effects of the medium,  $\mathbf{M}_R$  accounts for the effects of linear birefringence and optical activity and  $\mathbf{M}_D$  includes the effects of linear and circular diattenuations (or dichroism). The algebraic details for this decomposition analysis can be found in [19] and in our previous publications [11–13].

An interesting problem that arises is the fact that the multiplication order in eq. (2) is potentially ambiguous (due to the non-commuting nature of matrix multiplication,  $\mathbf{M}_A \mathbf{M}_B \neq \mathbf{M}_B \mathbf{M}_A$ ), so that six different orders of multiplications are

possible. The six different decompositions are classified into two families, depending upon the location of the matrices for the depolarizer and the diattenuator [20]. The three decompositions with the depolarizer located after the diattenuator form the first family (in which eq. (2) belongs). On the other hand, the three decompositions with the depolarizer set before the diattenuator constitute the other family.

$$\begin{array}{ccc}
 & (\mathbf{M}_{\Delta D} \text{ family}) & (\mathbf{M}_{D\Delta} \text{ family}) \\
 \mathbf{M} & \begin{array}{l} \swarrow \mathbf{M}_{\Delta} \mathbf{M}_R \mathbf{M}_D \text{ (3.1)} \\ \rightarrow \mathbf{M}_{\Delta} \mathbf{M}_D \mathbf{M}_R \text{ (3.2)} \\ \searrow \mathbf{M}_R \mathbf{M}_{\Delta} \mathbf{M}_D \text{ (3.3)} \end{array} & \mathbf{M} \Leftarrow \begin{array}{l} \mathbf{M}_D \mathbf{M}_R \mathbf{M}_{\Delta} \text{ (3.4)} \\ \rightarrow \mathbf{M}_R \mathbf{M}_D \mathbf{M}_{\Delta} \text{ (3.5)} \\ \searrow \mathbf{M}_D \mathbf{M}_{\Delta} \mathbf{M}_R \text{ (3.6)} \end{array} .
 \end{array}$$

Among the six decompositions, algorithms for obtaining the basis matrices in eq. (3.1) or for its reverse order (eq. (3.4)), have been developed [19,21]. The other decompositions can be obtained using similarity transformations, for each of the two individual families [21]. In our analysis, we have thus used eqs (3.1) and (3.4) to decompose  $\mathbf{M}$  (experimental Mueller matrices or the MC-generated ones).

The decomposed basis matrices are further analysed to derive individual medium polarization properties. Specifically, diattenuation ( $d$ , differential attenuation of orthogonal polarizations for linear and for circular polarization states), depolarization coefficients ( $\Delta$ , linear and circular), linear retardance ( $\delta$ , difference in phase between two orthogonal linear polarizations), and circular retardance or optical rotation ( $\psi$ , difference in phase between right- and left-circularly polarized light), can be determined from the basis matrices.

The magnitude of diattenuation ( $d$ ) can be determined from [11,19]

$$d = \frac{1}{M_D(1,1)} \sqrt{M_D(1,2)^2 + M_D(1,3)^2 + M_D(1,4)^2}. \quad (4)$$

Here, the coefficients  $M_D(1,2)$  and  $M_D(1,3)$  represent linear diattenuation for horizontal (vertical) and  $+45^\circ$  ( $-45^\circ$ ) linear polarization states respectively, and the coefficient  $M_D(1,4)$  represents circular diattenuation.

In the next step, depolarization is quantified from the depolarization matrix  $\mathbf{M}_{\Delta}$  as the net depolarization coefficient  $\Delta$ , linear retardance  $\delta$  and optical rotation  $\psi$  are calculated from the elements of the retarder matrix  $\mathbf{M}_R$  [11]. Specifically,

$$\Delta = 1 \frac{|\text{tr}(\mathbf{M}_{\Delta}) - 1|}{3} \quad (5)$$

$$\delta = \cos^{-1} \left( \sqrt{(\mathbf{M}_R(2,2) + \mathbf{M}_R(3,3))^2 + (\mathbf{M}_R(3,2) - \mathbf{M}_R(2,3))^2} - 1 \right) \quad (6)$$

$$\psi = \tan^{-1} \left( \frac{\mathbf{M}_R(3,2) - \mathbf{M}_R(2,3)}{\mathbf{M}_R(2,2) + \mathbf{M}_R(3,3)} \right). \quad (7)$$

### 3. Results and discussions

#### 3.1 Selected results on validation of the Mueller matrix decomposition method in complex turbid media

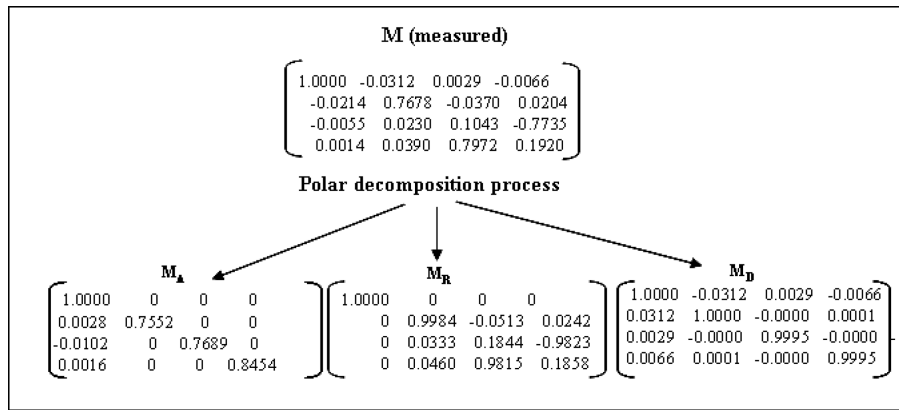
Prior to exploring the use of the extended Mueller matrix decomposition methodology in actual tissues, its validity was tested in tissue-like turbid media (whose constituent properties are known and user-controlled *a priori*) with both experimental and MC-simulated Mueller matrices [11,12].

In the experimental studies, the PEM-based polarimeter [11] was used to record Mueller matrices in the forward detection geometry (sample thickness = 1 cm, detection area of 1 mm<sup>2</sup> and an acceptance angle of  $\sim 20^\circ$  around were used) from a solid polyacrylamide phantom that mimics the complexity of biological tissues, in that it exhibits simultaneous linear birefringence, optical activity and depolarization. These solid optical phantoms (dimension of  $1 \times 1 \times 4$  cm) were developed using polyacrylamide as a base medium, with sucrose-induced optical activity, polystyrene microspheres-induced (mean diameter  $D = 1.40 \mu\text{m}$ , refractive index  $n_s = 1.59$ ) scattering and mechanical stretching to cause linear birefringence. The phantoms were stretched along the vertical direction (along the long axis of the sample) to introduce varying linear birefringence. Complete experimental control of polarizing effects of all constituent sample was thus available.

Table 1 shows the experimental Mueller matrix and the corresponding decomposed  $\mathbf{M}_\Delta$ ,  $\mathbf{M}_R$  and  $\mathbf{M}_D$  matrices from a birefringent (extension = 4 mm), chiral (optical activity  $\chi = 1.96^\circ/\text{cm}$ , corresponding to 1 M concentration of sucrose), turbid phantom ( $\mu_s = 30 \text{ cm}^{-1}$  and average cosine of scattering angle  $g = 0.95$ ). The complex nature of the recorded Mueller matrix  $\mathbf{M}$ , with essentially all the 16 non-zero elements, underscores the problem – how does one extract useful sample metrics from this intertwined information? In contrast, the three basis matrices derived from the decomposition process exhibit simpler features with many of the off-diagonal elements being zero. These are thus directly amenable for further quantification. The individual polarization parameters ( $d$ ,  $\Delta$ ,  $\delta$  and  $\psi$ ) were retrieved by applying eqs (4)–(7) to the decomposed basis matrices. The determined values for these are also listed in table 1, showing excellent agreement with the controlled inputs.

The values for  $\delta$  and  $\psi$  determined from the decomposition of the measured Mueller matrices in both non-scattering (no microspheres) and turbid ( $\mu_s = 30 \text{ cm}^{-1}$ ,  $g = 0.95$ ) optically active ( $\chi = 1.96^\circ/\text{cm}$ ) phantoms with increasing birefringence (sample extension of 0–4 mm,  $\delta = 0$ –1.34 rad), are displayed in figure 2a. The values from both clear and scattering samples are observed to be in close agreement with the controlled experimental inputs ( $\psi \approx 1.96^\circ$  and  $\delta \approx 1.34$  rad at 4 mm of extension). This suggests that the depolarizing effects of multiple scattering have been properly isolated and accounted for. Figure 2b shows the derived linear retardance  $\delta$  and optical rotation  $\psi$  parameters, using Monte Carlo-generated Mueller matrices and with chiral molecule concentration as the independent variable. Again, both the non-scattering and turbid values compare well with the input parameters ( $\delta \approx 1.4$  rad and  $\psi \approx 1.96^\circ$  at 1 M sucrose), showing self-consistency in inverse decomposition analysis and successful decoupling. The observed small

**Table 1.** (Top): The experimentally recorded Mueller matrix and the decomposed matrices for a birefringent (extension = 4 mm), chiral (sucrose concentration = 1 M,  $\chi = 1.96^\circ \text{ cm}^{-1}$ ), turbid ( $\mu_s = 30 \text{ cm}^{-1}$ ,  $g = 0.95$ , thickness = 1 cm) phantom. (Bottom): The values for the extracted polarization parameters are shown in the 2nd column. The control input values for  $\delta$  and  $\psi$  (expected values shown in the 3rd column) were obtained from the measurement on a non-scattering ( $\mu_s = 0 \text{ cm}^{-1}$ ) phantom having the same extension (= 4 mm) and similar concentration of sucrose (1 M) as that of the turbid phantom. The expected values are corrected for the increased path-length due to multiple scattering (determined from Monte Carlo simulation). The expected value for the net depolarization coefficient  $\Delta$  was determined from the Monte Carlo simulation of the experiment (adopted from ref. [26]).



Parameters	Estimated value (derived from Mueller matrix decomposition)	Expected value
$d$ (unitless)	0.03	0
$\delta$ (radian)	1.38	1.34
$\psi$ (degree)	2.04	$2.07^\circ$
$\Delta$ (unitless)	0.21	$\sim 0.2$

increases in optical rotation in the presence of turbidity (in either the experimental phantoms or the analogous MC-simulated turbid media) are caused by the increase in optical pathlength due to multiple scattering (resulting in the accumulations of  $\psi$  values) [11,13].

In contrast to the forward detection geometry, determination of the intrinsic polarization parameters in the backward detection geometry is more complex because the scattering-induced artifacts are more coupled with the intrinsic parameters due to the contribution of the singly or weakly backscattered photons [12]. For example, backscattering-induced changes in the orientation angle of the linear polarization vector can manifest themselves as large apparent optical rotation even in the absence of intrinsic chirality [7,8]. Decomposition analysis revealed that this



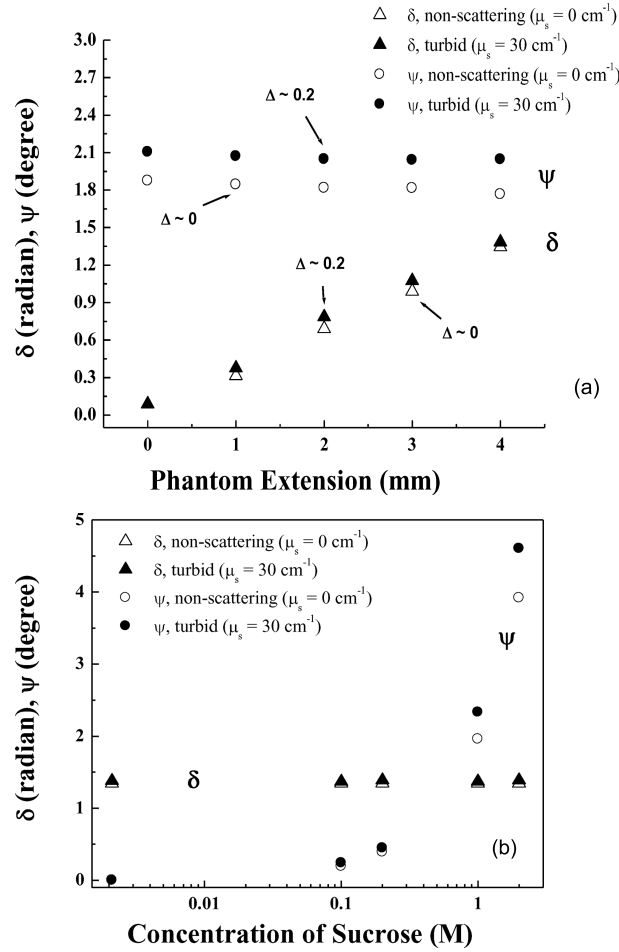


**Figure 2.** (a) Linear retardance  $\delta$  (triangle) and optical rotation  $\psi$  (circle) determined from experimental Mueller matrices of chiral ( $\chi = 1.96^\circ \text{ cm}^{-1}$ , corresponding to 1 M concentration of sucrose) phantoms having varying magnitudes of birefringence (induced by extension of phantoms 0–4 mm,  $\delta = 0$ –1.345 radian). Results are shown for both non-scattering (open symbols,  $\mu_s = 0 \text{ cm}^{-1}$ ) and turbid (solid symbols,  $\mu_s = 30 \text{ cm}^{-1}$ , average cosine of scattering angle  $g = 0.95$ ) phantoms. The measurements were performed in the forward direction (detection angle =  $0^\circ$ ) through a  $1 \text{ cm} \times 1 \text{ cm} \times 4 \text{ cm}$  phantom (adopted from ref. [13]). (b)  $\delta$  (triangle) and  $\psi$  (circle) determined from the decomposition of Monte Carlo-generated Mueller matrices from birefringent media magnitude of linear birefringence  $\Delta n = 1.36 \times 10^{-5}$ , corresponding to  $\delta = 1.345$  radian (analogous to 4 mm extension of 4 cm long experimental phantom) for a path length of 1 cm, having varying amount of chirality ( $\chi = 0, 0.196, 0.392, 1.96$  and  $3.92^\circ \text{ cm}^{-1}$ , corresponding to the sucrose concentration of 0, 0.1, 0.2, 1 and 2 M, respectively). Results are shown for both non-scattering (open symbols,  $\mu_s = 0 \text{ cm}^{-1}$ ) and turbid (solid symbols,  $\mu_s = 30 \text{ cm}^{-1}$ ,  $g = 0.95$ ) media (adopted from ref. [13]).

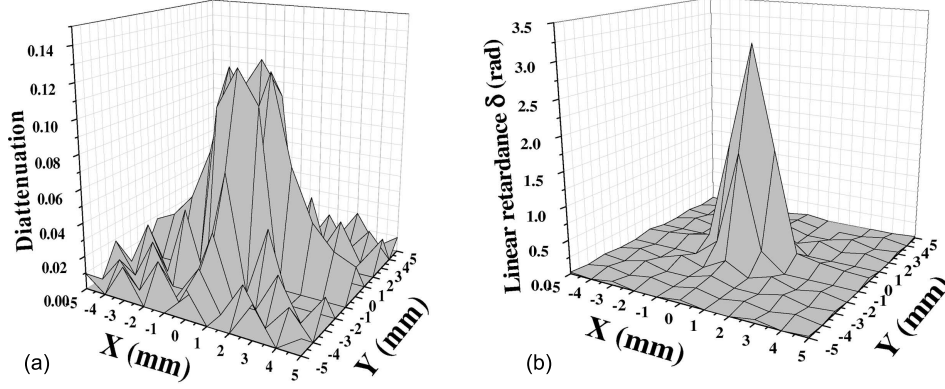


**Figure 3.** (a) Linear diattenuation  $d$  (unitless) and (b) linear retardance  $\delta$  (in radian) maps in the backscattering plane ( $X$ - $Y$  plane,  $Z = 0$ ) determined using decomposition of Monte Carlo-generated Mueller matrices of a non-birefringent ( $\Delta n = 0$ ), achiral ( $\chi = 0^\circ \text{ cm}^{-1}$ ), turbid medium ( $\mu_s = 60 \text{ cm}^{-1}$ ,  $g = 0.935$ ).

large apparent rotation is due to scattering-induced linear diattenuation (difference in amplitude between the scattered light polarized parallel and perpendicular to the scattering plane) [11–13]. In addition to diattenuation, backscattered photons yield significant linear retardance (differences in phase between the scattered light polarized parallel and perpendicular to the scattering plane) even from isotropic ( $\Delta n = 0$ ) scattering medium [12]. This interferes with the actual retardance values of a birefringent turbid medium in a complex fashion, thus hindering the determination of the latter in the backward detection geometry. We have therefore investigated this aspect also. As these scattering-induced diattenuation and linear retardance are due mainly to the singly (or weakly) backscattered photons, their magnitudes gradually diminish as one moves away from the exact backscattering direction. Specifically, beyond a transport length away from the point of illumination ( $r > l_{tr}$ ,  $l_{tr}$  is the transport scattering length  $= 1/\mu_s(1 - g)$ ), these confounding effects become very weak [12]. This is illustrated in figures 3a and 3b, where the scattering-induced diattenuation ( $d$ ) and linear retardance ( $\delta$ ) maps in the backscattering plane ( $X$ - $Y$  plane,  $Z = 0$ ) are shown from an isotropic ( $\Delta n = 0$ ), achiral ( $\chi = 0^\circ \text{ cm}^{-1}$ ), turbid medium ( $\mu_s = 60 \text{ cm}^{-1}$ ,  $g = 0.935$ , thickness = 1 cm). These suggest that simultaneous determination of the intrinsic values of all the polarization parameters from a turbid medium in the backward detection geometry can be accomplished by recording Mueller matrix at a distance larger than the transport length away from the point of illumination [12].

The studies conducted on the influence of the order of the matrices in the decomposition analysis on the retrieved polarization parameters confirmed that the decomposition formalism is self-consistent with respect to the potential ambiguity of ordering of the constituent matrices [22]. Thus it appears that the polar decomposition analysis enables successful decoupling and quantification of the individual, intrinsic polarimetry characteristics in complex random medium, despite their simultaneous occurrence, even in the presence of the numerous complexities due to

multiple scattering. In the following, we discuss initial biomedical applications of this promising approach.

### *3.2 Monitoring stem cell-based regenerative treatments of the heart*

Mueller matrix decomposition method was explored for polarimetric monitoring of the regeneration of myocardial tissues following stem-cell therapy. The anisotropic organized nature of myocardial tissues originating from their fibrous structure leads to linear birefringence. After an infarction (heart attack), a portion of the myocardium is deprived of oxygenated blood and subsequently cardiomyocytes die, being replaced by isotropic scar tissues. Stem-cell-based regenerative treatments for myocardial infarction have shown to reverse this trend by increasing the muscular and decreasing the scar tissue components [23]. These processes are expected to affect linear birefringence and its measurement may offer a sensitive probe into the state of the myocardium after infarction and report on the success of regenerative treatments. In order to explore this possibility, Mueller matrix measurement and its decomposition was performed to decouple and quantify the small birefringence alterations (as a signature of tissue status) of the myocardial tissues.

Mueller matrices were recorded in the transmission geometry, from 1-mm thick *ex vivo* myocardial samples from Lewis rats after myocardial infarction, both with and without stem-cell treatments [13,24,25]. Measurements were made using both the point measurement and imaging polarimetry systems (described in §2.1). The Mueller matrices measured by either of these systems were analysed by polar decomposition to obtain linear retardance ( $\delta$ ) values. The results are summarized in figure 4. A large decrease in the magnitude of  $\delta$  is seen in the infarcted region of the untreated myocardium (figure 4b). In contrast, in the infarcted region after stem-cell treatment an increase in  $\delta$  towards the native levels can be observed (figure 4b), indicating re-growth and re-organization of the myocardium. The polarimetry images (figure 4c) from the same tissue also show similar retardance trends as seen in the point measurement results, although some variations are seen (due to difference in measurement geometry and spatial heterogeneity in tissue optics). In the spatial variation of the retardance images (figure 4c), not only do the values change from infarct to normal, but also within each region. In general, the  $\delta$  values are higher in the middle of the myocardial wall with values gradually lowering towards the edges. This variation may be due to the change in orientation of the myocyte fibres through the wall. Note that the fibre orientation undergoes a rotation of  $180^\circ$  from outside the ventricle to the inside. Whereas in the inside and outside of the ventricle the fibres are oriented perpendicular to the axial imaging plane, in the central region, the fibres are parallel to the imaging plane. As the axis of birefringence (direction of the fibres) is along the direction of the light's propagation, the corresponding retardance values in the outside and inside walls are generally lower. Reverse is the case (birefringence axis perpendicular to light propagation direction) in the central region, leading to larger magnitude of the observed  $\delta$ .

Nevertheless, statistically significant ( $p < 0.05$ ) differences in derived retardance values were obtained between normal and infarcted regions, and between infarcted regions with and without stem-cell treatments (shown in figure 5). The retardance

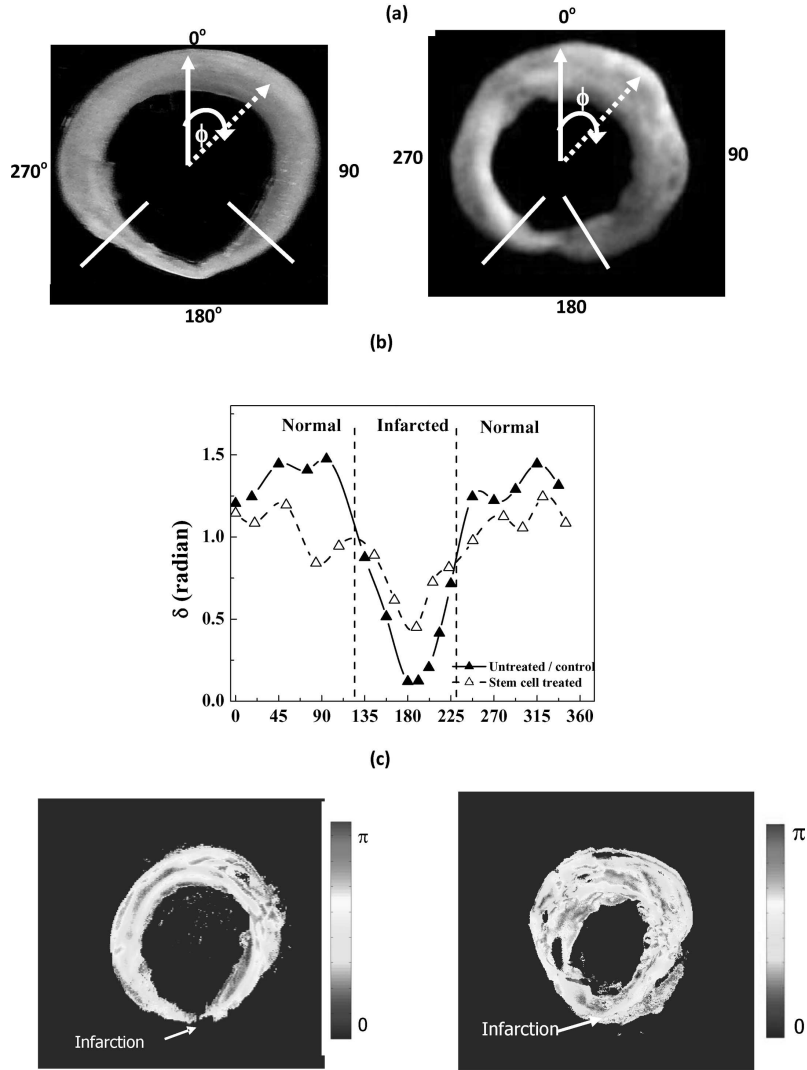


**Figure 4.** Linear retardance  $\delta$  derived from Mueller matrix measurements in 1-mm-thick tissue sections from Lewis rat hearts following myocardial infarction. (a) White-light photographs of untreated (left panel) and stem cell-treated (right panel) tissue. The marked sectors around  $\varphi = 180^\circ$  show the infarcted regions. (b) Mueller matrix-derived linear retardance ( $\delta$ ) values at different angular positions from the untreated ( $\blacktriangle$ ) and treated ( $\triangle$ ) samples. (c) The corresponding linear retardance ( $\delta$ ) images for the same tissue derived from the imaging polarimetry measurements.

is significantly reduced in the region of infarction and increases through the marginal region to higher levels in un-infracted tissues. In addition, the retardance in the region of infarction increases with treatment. This increase in  $\delta$  in the in-

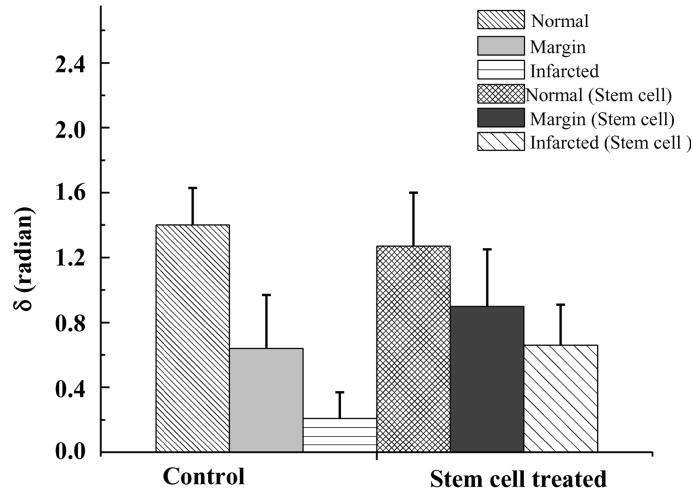


**Figure 5.** The results from linear retardance measurements from the controls and the stem cell-treated groups of infarcted hearts are shown in the histogram. The results are shown from healthy, marginal and infarcted regions. The error bars are the standard deviation.

farcted regions of the treated hearts indicates reorganization and regrowth of the myocardium (this was confirmed by histologic examination). These results show promise for the use of polarized light monitoring of stem cell-based treatments of myocardial infarction, and our current work is directed towards extending this novel method for *in vivo* biomedical deployment.

### 3.3 *In vivo* tissue structural anisotropy monitoring

The first *in vivo* use of the Mueller matrix decomposition method for tissue characterization was demonstrated using a dorsal skin-fold window chamber mouse model [14]. In this model, the skin layer of an athymic nude mouse (NCRNU-M, Taconic) was removed from a 10 mm diameter region on the dorsal surface, and a titanium saddle was sutured in place to hold the skin flap vertically. A protective glass coverslip ( $145 \pm 15 \mu\text{m}$  thick) was placed over the exposed tissue plane (shown in figure 6a). *In vivo* optical transmission Mueller matrix measurements were performed through the  $\sim 500 \mu\text{m}$  thick tissue layer.

Collagenase was injected into a region of the tissue to alter the structure of the extra-cellular matrix. Measurements were performed both from the region of collagenase injection and a distant control region. Measurements were made before collagenase treatment and at different times after the treatment. Values for linear retardance ( $\delta$ ) and net depolarization coefficient ( $\Delta$ ) were extracted from the experimentally-derived Mueller matrices at each time point, using the matrix decomposition approach [14]. The derived variations of  $\delta$  and  $\Delta$  (in both control and treated regions) are shown as a function of time, in figures 6b and 6c respectively.

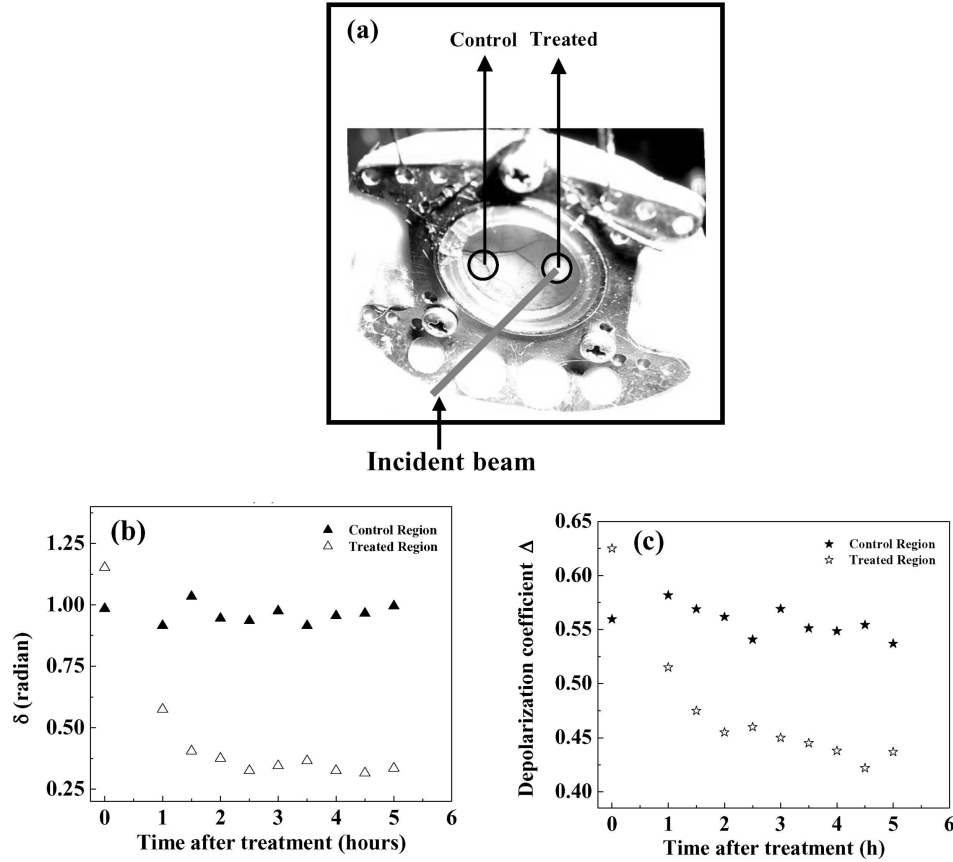


**Figure 6.** (a) Photograph of the skin-fold window chamber mouse model. The two measurement regions (collagenase-treated and control) are marked in the photograph. Mueller matrix-derived values for (b) linear retardance  $\delta$  and (c) depolarization coefficient  $\Delta$  before and as a function of time after collagenase injection in the treated and control regions. The Mueller matrices were recorded in the forward detection angle using the point polarimetry measurement system (adopted from ref. [14]).

The value for  $\delta$  is observed to vary from  $\delta \approx 1.2$  rad to  $\delta \approx 0.3$  rad in the treated region, whereas in the control region the values remain essentially constant ( $\delta \approx 1$  rad). This decrease in birefringence is due to denaturation of the collagen fibres (collagenase cleaves the collagen fibres by breaking the peptide bonds connecting the monomer peptide units), which reduces the tissue structural anisotropy (this was confirmed by histology). Note that the observed variation in  $\delta$  is also associated with a decrease in the net depolarization coefficient  $\Delta$  after treatment from  $\sim 0.63$  to  $\sim 0.45$  (figure 6b). The values in the control region were again observed to remain essentially constant. This reduction in  $\Delta$  is also due to the cleavage of the collagen fibres, as these fibres are one of the primary scattering structures in tissue. In fact, using these changes in  $\delta$  and  $\Delta$  parameters, we were able to estimate the

intrinsic birefringence ( $\Delta n$ ) and scattering coefficient ( $\mu_s$ ) values, with the aid of the polarization-sensitive Monte Carlo simulations [14]. The values for  $\mu_s$  were found to be  $182 \text{ cm}^{-1}$  for the pre-treatment tissue and  $134 \text{ cm}^{-1}$  for the post-treatment tissue, which are in reasonable agreement with literature values. These results demonstrated the ability of the method to quantify changes in tissue structure *in vivo*.

#### 4. Concluding remarks

To conclude, a novel general method for polarimetry analysis in turbid media based on polar Mueller matrix decomposition has been developed and validated. The ability to isolate individual polarization properties in complex random media (such as tissues) provides a valuable noninvasive tool for their characterization. In the biological domain, quantification of tissue structural anisotropy via birefringence may be useful for a variety of diagnostic/therapeutic applications. Monitoring regenerative treatment of heart is an important potential application that has been initially explored, with early indications showing promise and warranting further studies. Initial studies on the use of this approach for quantification of optical rotation caused by chiral molecules in turbid medium (like for example glucose in human tissue), have also yielded very encouraging results (not presented in this paper) and demonstrated that indeed the approach can isolate the small optical rotation caused exclusively by chiral molecules from the (often much larger) apparent rotation caused by the scattering/detection geometry effects. In combination with MC-determined pathlength distributions, we are currently investigating methods for extracting chiral molecule concentrations from the derived optical rotations [26–28]. Clearly, there are many other potential applications in biomedicine, both in tissue diagnostics and in treatment response monitoring.

#### References

- [1] R R Kortum and E Servick-Muraca, *Annu. Rev. Phys. Chem.* **47**, 556 (1996)
- [2] G A Wagnieres, W M Star and B C Wilson, *Photochem. Photobiol.* **68**, 603 (1998)
- [3] L V Wang, G L Côté and S L Jacques, *J. Biomed. Opt.* **7**, 278 (2002)
- [4] J F de Boer and T E Milner, *J. Biomed. Opt.* **7**, 359 (2002)
- [5] K Schoenenberger, B W Colston Jr, D J Maitland, L B Da Silva and M J Everett, *Appl. Opt.* **37**, 6026 (1998)
- [6] R J McNichols and G L Cote, *J. Biomed. Opt.* **5**, 5 (2000)
- [7] D Côté and I A Vitkin, *Opt. Exp.* **13**, 148 (2005)
- [8] S Manhas, M K Swami, P Buddhiwant, N Ghosh, P K Gupta and K Singh, *Opt. Exp.* **14**, 190 (2006)
- [9] R A Chipman, Polarimetry, Chap. 22 in: *Handbook of optics*, 2nd edn, edited by M Bass (McGraw-Hill, New York, 1994) Vol. 2, pp. 22.1–22.37
- [10] C Brosseau, *Fundamentals of polarized light: A statistical optics approach* (Wiley, New York, 1998)
- [11] N Ghosh, M F G Wood and I A Vitkin, *J. Biomed. Opt.* **13**, 044036 (2008)
- [12] N Ghosh, M F G Wood and I A Vitkin, *J. Appl. Phys.* **105**, 102023 (2009)

- [13] N Ghosh, M F G Wood, Shu-hong Li, R D Weisel, B C Wilson, Ren-Ke Li and I A Vitkin, *J. Biophoton.* **2**, 145 (2009)
- [14] M F G Wood, N Ghosh, E H Moriyama, B C Wilson and I A Vitkin, *J. Biomed. Opt.* **14**, 014029 (2009)
- [15] X Guo, M F G Wood and I A Vitkin, *J. Biomed. Opt.* **11**, 041105 (2006)
- [16] A J Welch and M J C van Gemert, *Optical-thermal response of laser irradiated tissue* (Plenum Press, New York, 1995)
- [17] C F Bohren and D R Huffman, *Absorption and scattering of light by small particles* (Wiley, New York, 1983) Chap. 2
- [18] M F G Wood, X Guo and I A Vitkin, *J. Biomed. Opt.* **12**, 014029 (2007)
- [19] S Yau Lu and R A Chipman, *J. Opt. Soc. Am.* **A13**, 1106 (1996)
- [20] J Morio and F Goudail, *Opt. Lett.* **29**, 2234 (2004)
- [21] R Ossikovski, A De Martino and S Guyot, *Opt. Lett.* **32**, 689 (2007)
- [22] N Ghosh, M F G Wood and I A Vitkin, *Opt. Commun.* **283**, 1200 (2010)
- [23] Y Sun, J Q Zhang, J Zhang and S Lamparter, *J. Lab. Clin. Med.* **135**, 316 (2000)
- [24] M A Wallenburg, M Pop, M F G Wood, N Ghosh, G A Wright and I A Vitkin, *J. Innovative Optical Health Sciences* **3**, 109 (2010)
- [25] M F G Wood, N Ghosh, M A Wallenburg, Shu-Hong Li, R D Weisel, B C Wilson, Ren-Ki Li and I A Vitkin, *J. Biomed. Opt.* **15**, 047009 (2010)
- [26] N Ghosh, M Wood and I A Vitkin, Polarized light assessment of complex turbid media such as biological tissues using Mueller matrix decomposition, Chapter 9, *Handbook of photonics for biomedical science* edited by Valery V Tuchin (Taylor and Francis Publishing, USA, 2010) pp. 253–282
- [27] M F G Wood, N Ghosh, Xinxin Guo and I A Vitkin, Towards noninvasive glucose sensing using polarization analysis of multiply scattered light, Chapter 17, *Handbook of optical sensing of glucose in biological fluids and tissues* edited by Valery V Tuchin, Series in Medical Physics and Biomedical Engineering (Taylor and Francis Publishing, 2008) Vol. 12
- [28] M A Wallenburg, M F G Wood, N Ghosh and I A Vitkin, *Opt. Lett.* **35**, 2570 (2010)